

# Nanoscale

Accepted Manuscript



This is an *Accepted Manuscript*, which has been through the Royal Society of Chemistry peer review process and has been accepted for publication.

*Accepted Manuscripts* are published online shortly after acceptance, before technical editing, formatting and proof reading. Using this free service, authors can make their results available to the community, in citable form, before we publish the edited article. We will replace this *Accepted Manuscript* with the edited and formatted *Advance Article* as soon as it is available.

You can find more information about *Accepted Manuscripts* in the [Information for Authors](#).

Please note that technical editing may introduce minor changes to the text and/or graphics, which may alter content. The journal's standard [Terms & Conditions](#) and the [Ethical guidelines](#) still apply. In no event shall the Royal Society of Chemistry be held responsible for any errors or omissions in this *Accepted Manuscript* or any consequences arising from the use of any information it contains.

# Anomalous Optical and Magnetic Behavior of Multi-Phase Mn Doped Zn<sub>2</sub>SiO<sub>4</sub> Nanowires: A New Class of Dilute Magnetic Semiconductors

Muhammad Hafeez<sup>1</sup>, Awais Ali<sup>1</sup>, Sadia Manzoor<sup>1,2</sup>, and Arshad S. Bhatti<sup>1,\*</sup>

<sup>1</sup>Centre for Micro and Nano Devices, Department of Physics, COMSATS Institute of Information Technology, Islamabad 44000. PAKISTAN

<sup>2</sup>Magnetism laboratory, Department of Physics, COMSATS Institute of Information Technology, Islamabad 44000. PAKISTAN

\*Contact author e-mail: [asbhatti@comsats.edu.pk](mailto:asbhatti@comsats.edu.pk)

## Abstract:

We present the synthesis of Mn doped Zn<sub>2</sub>SiO<sub>4</sub> dense nanowire bundles using VLS mode of growth with unusual optical and magnetic properties. The synthesized Zn<sub>2</sub>SiO<sub>4</sub> nanowires were identified with two phases,  $\alpha$ -Zn<sub>2</sub>SiO<sub>4</sub> as the major phase and  $\beta$ -Zn<sub>2</sub>SiO<sub>4</sub> as the minor phase. XPS studies confirmed that Zn<sub>2</sub>SiO<sub>4</sub> nanowires were Zn rich and Mn doped. Temperature dependent photoluminescence (PL) measurements showed three distinct emission bands: green, yellow and red due to Mn doping in the  $\alpha$ -phase,  $\beta$ -phase and the substitution of Si with Mn in the  $\alpha$ -phase, respectively). The PL analysis showed that these emission bands followed anomalous Berthelot-type behavior. The carrier escape energies were  $70 \pm 3$  meV,  $49 \pm 2$  meV and  $65 \pm 4$  meV for the 530, 570 and 660 nm bands, respectively while the radiation rates ( $E_r =$ ) were  $1.0 \pm 0.4$  meV,  $3.10 \pm 1.10$  meV and  $1.4 \pm 0.4$  meV corresponded to the three respective bands. Mn doping of Zn<sub>2</sub>SiO<sub>4</sub> nanowires induced ferromagnetism, which was observed above room temperature, with a Curie temperature well above 380 K. Observation of magnetic behavior in this class of semiconductors has potential applications in high temperature spintronics and magneto-optical devices.

**Keywords:** Wide band gap semiconductors; dilute magnetic semiconductor; photoluminescence (PL) spectroscopy; X-ray photoemission spectroscopy (XPS); ferromagnetism

## I. Introduction:

In recent years, research in one dimensional (1-D) nanostructures, such as nanorods, nanowires, nanobelts, and nanotubes, has become intense due to growing technological demands of smaller, more efficient and powerful devices [1-5]. The unique characteristics of 1-D nanostructures are attributed to the quantum confinement effect, which has led to band gap engineering [6-10].

A broad range of 1-D oxide semiconductor nanostructures has attained much attention due to their use in electronic and photonic devices [11-12]. With a wide band gap of 5.5 eV, zinc silicate ( $\text{Zn}_2\text{SiO}_4$ ) is a promising multifunctional material with proven applications as a phosphor host in medical imaging, in cathode ray tubes, electronic insulators, paints and fluorescent lamps [13-15]. Recently, 1-D  $\text{Zn}_2\text{SiO}_4$  nanostructures, such as nanowires and nanorods were fabricated and their optical, chemical, water purification and sensing properties studied [16-18]. Willemite ( $\text{Zn}_2\text{SiO}_4$ ) is a well-known host material for applications in the field of phosphors for light emitting devices [19]. It can emit in blue, green and red colors when doped with  $\text{Eu}^{3+}$ ,  $\text{Mn}^{2+}$  and  $\text{Ce}^{3+}$  ions, respectively [20-22].  $\text{Zn}_2\text{SiO}_4$  emits green and yellow colors when  $\text{Mn}^{2+}$  ions are doped in the  $\alpha$ - and  $\beta$ -phases  $\text{Zn}_2\text{SiO}_4$ , respectively, where Mn replaces Zn in the willemite structure [23]. It has been found that amount of  $\text{Mn}^{2+}$  doping affects the luminescence properties of  $\text{Zn}_2\text{SiO}_4$ . The states involved in the luminescence could be from isolated  $\text{Mn}^{2+}$  ions or magnetically coupled isolated paired  $\text{Mn}^{2+}$  ions. The formation of paired  $\text{Mn}^{2+}$  ions magnetically coupled depend strongly on the concentration of  $\text{Mn}^{2+}$  ions. The decay times for luminescence is long ( $\sim 10$ -15 ms) (short ( $\sim 1$ -2 ms)) for isolated (isolated coupled or paired)  $\text{Mn}^{2+}$  ions, respectively, [24, 25]. The variation in the decay times, which is one order of magnitude, affects the luminescence characteristics of zinc silicate. In addition, intrinsic defects have also been found in  $\text{Zn}_2\text{SiO}_4$  due to Si and O vacancies, which have led to creation of shallow defect states, which act as charge traps or carrier reservoirs [26], which can be depopulated at high temperatures. This has made it a potentially interesting material for devices with high luminescence efficiency. Due to interesting optical properties of Mn doped  $\text{Zn}_2\text{SiO}_4$ , many groups have studied the effect of Mn concentration on PL and phase stabilization [19, 23, 27-29]. However, no extensive study of the magnetic behavior has been reported of such systems to date.

It is expected that doping of Mn in low concentrations in the host  $\text{Zn}_2\text{SiO}_4$  should introduce dilute magnetic semiconductor (DMS) behavior in the system.

There are various methods for the synthesis of  $\text{Zn}_2\text{SiO}_4$  nanostructures, namely, sol-gel method, hydrothermal and solvo-thermal methods, supercritical water methods and the vapor phase method [30-35]. Among these, the vapor phase method is the simplest way to get high density and high quality single crystalline 1-D  $\text{Zn}_2\text{SiO}_4$  nanostructures. A further advantage of this method is that the morphology of the  $\text{Zn}_2\text{SiO}_4$  nanostructures can be changed from nanoparticles to nanospheres, nanorods, nanoneedles and nanowires by changing the growth temperature and precursor material [36].

In this paper, we report a novel way to synthesize Mn doped  $\text{Zn}_2\text{SiO}_4$  nanowire bundles by using two sources of vapor species, i.e.,  $\text{MnCl}_2$  and  $\text{ZnS}$ , while using Si substrate as the source of Si. Scanning electron microscopy (SEM) and high resolution transmission electron microscopy (HRTEM) were used to study the morphology and dimensions of the grown nanostructures. Selected area electron diffraction pattern (SAED), X-ray diffraction (XRD) and X-ray photoelectron spectroscopy (XPS) were used to determine the structure and composition of the as grown nanowires. Temperature dependent PL measurements exhibited the Berthelot-type behavior of the band gap defect states. The Berthelot type behavior has already been reported in chalcogenide glasses, InGaN/GaN semiconductor heterosystems, Ge quantum dots, amorphous silicon, siloxene and amorphous hydrogenated silicon (*a*-Si:H) [37-41], where band tail states participate in the recombination of electron hole pairs. We also report the first time observation of magnetization behavior in the Mn doped  $\text{Zn}_2\text{SiO}_4$  nanowires and found that it corresponded to that of a typical DMS system.

## II. Experiment:

Si (100) substrates with an ultrathin (2-3 nm) native oxide layer were used for the growth of nanostructures. 1 nm Sn thin film was first deposited in an ultra high vacuum chamber at room temperature. 99.99% pure  $\text{ZnS}$  powder (1g) and  $\text{MnCl}_2 \cdot 8\text{H}_2\text{O}$  (0.5g) were used as source materials in separate alumina boats.  $\text{MnCl}_2$  powder was placed in the upstream zone of the tube furnace before the  $\text{ZnS}$  powder about 20 cm away from the center of the furnace. A number of substrates were placed in the downstream zone at 850°C. The furnace was then heated to 1120°C at a rate of 60°C/hr in the presence of flowing  $\text{N}_2+5\% \text{H}_2$  gas (at a rate of 20 Sccm) to transport

vapors from the source boat to the Si substrates. The growth was done for two hours and then the synthesized nanostructures were furnace cooled in the present of flowing carrier gas.

The synthesized nanostructures were characterized by a field emission scanning electron microscope (SEM) (Hitachi SU 8000), high-resolution transmission electron microscope (HRTEM, JEM-2100F) equipped with an x-ray energy dispersive spectrometer (EDS), and X-ray diffractometer (XRD) (RINT 2200HF) for analyzing the morphology, crystal structure and phase identification, respectively. Temperature dependent PL measurements were done by the Lab RamIII (Dongwoo Optron) in the closed cycle He cryostat. Excitation for the PL spectroscopy was performed with an argon ion laser at 488 nm. Magnetic measurements were made using the Quantum Design VersaLab VSM in the temperature range 60 – 380 K.

### III. Results and Discussion

#### a. Morphology, Phase and Elemental Analysis:

Figure 1 (a–d) shows low and high magnification SEM and TEM micrographs of the  $\text{Zn}_2\text{SiO}_4$  nanowire bundles. The grown nanostructures were dense, aligned  $\text{Zn}_2\text{SiO}_4$  nanowire arrays/bundles with an average diameter in the range of 40 to 80 nm and average length of a few micrometers (Figure 1 (a and b)). Figure 1 (c) and (d) shows the TEM and HRTEM images of  $\text{Zn}_2\text{SiO}_4$  nanowires and an individual nanowire, respectively. The HRTEM image revealed that the nanowire was single crystalline with [410] as the growth direction. A selected area electron diffraction (SAED) pattern further confirmed that the wire growth was along the [410] direction and also indicated the coexistence of the two phases,  $\alpha$ - and  $\beta$ - $\text{Zn}_2\text{SiO}_4$ , as shown in the inset of Figure 1 (d). The images for various constituents of nanostructures as obtained using energy dispersive X-ray spectroscopy mapping (Figure 2 (a)) revealed the amount of each constituent elements in the as grown nanostructures. The images taken in the bright field (BF) mode showed separately identifiable signatures of Cu, Zn, Si, O and Mn as bright spots. It was clear from the EDS mapping that the  $\text{Zn}_2\text{SiO}_4$  nanowires were rich in Zn and in addition it also showed presence of a small amount of Mn in the nanostructures. It is to be noted that Cu signal came from the TEM grid, while Sn, which was expected to act as a catalyst was not detected at all. The findings were unexpected, i.e., synthesis of dense aligned nanowires, formation of two phases of  $\text{Zn}_2\text{SiO}_4$  and doping of Mn. Thus it was imperative to determine the role of Mn in this unusual growth and its role in formation of two phases of  $\text{Zn}_2\text{SiO}_4$ . The quantification of various

observed phases formed during the growth was done by X-ray diffraction as discussed in the following.

Figure 2 (b) shows the XRD pattern of  $\text{Zn}_2\text{SiO}_4$  nanowires. All identified diffraction peaks were found to belong to willemite  $\text{Zn}_2\text{SiO}_4$  with lattice parameters  $a = b = 13.938 \text{ \AA}$  and  $c = 9.31 \text{ \AA}$ , (matched well with the literature and JCPDF # 37-1485). The narrow full width at half maximum of the diffracted peaks reflected the good quality of the synthesized nanowires. The XRD pattern showed a strong reflection from the [410] plane, which also confirmed the growth direction, in accordance with the HRTEM observations. The detailed XRD analysis showed that the  $\text{Zn}_2\text{SiO}_4$  was present in two phases:  $\alpha\text{-Zn}_2\text{SiO}_4$  as the major phase (approximately 80%) and  $\beta\text{-Zn}_2\text{SiO}_4$  as the minor phase (approximately 20%). The relative content of  $\alpha(\beta)\text{-Zn}_2\text{SiO}_4$  from the XRD pattern was calculated from the relative intensity of the peaks from both phases in the XRD pattern, where % content of  $\alpha(\beta)$  – phase was calculated using  $\left\{ \frac{I_{\alpha(\beta)}}{I_{\alpha} + I_{\beta}} * 100 \right\}$ . Where,  $I_{\alpha(\beta)}$  is the total intensity of  $\alpha(\beta)$ -phase in the XRD pattern. This is shown as the magnified pattern in the range from  $28^\circ$  to  $40^\circ$  in the inset of Figure 2 (b). No other characteristic reflections of any other materials or phases were observed in the measured  $2\theta$  range, which showed the purity of the synthesized  $\text{Zn}_2\text{SiO}_4$  nanowires

The stoichiometry of the as-grown  $\text{Zn}_2\text{SiO}_4$  was determined by XPS analysis and Figure 3 (a-e) shows the (a) complete XPS spectra of  $\text{Zn}_2\text{SiO}_4$  nanowires arrays and the magnified spectrum in the binding energy range of its constituents (b) Zn ( $2p$ ), (c) O ( $1s$ ), (d) Si ( $2p$ ), and (e) Mn ( $2p$ ). The binding energies were corrected taking into account the specimen charging by referring to C ( $1s$ ) at 284.60 eV peak position. The complete survey spectrum also confirmed the purity of the synthesized  $\text{Zn}_2\text{SiO}_4$  nanowires as no other element was detected. The peaks were labeled with the origin of the transition for each element and summarized in Table I, which also shows the concentration percentage of Zn, Si, O and Mn in the Mn doped  $\text{Zn}_2\text{SiO}_4$  nanowire arrays. It was clear from the compositional analysis that Mn was considerably doped in the nanowires and there existed a lot of Si vacancies in the nanowires. The composition as derived from XPS confirmed that the synthesized product was  $\text{Zn}_{2.079}\text{Si}_{0.968}\text{O}_{3.792} \cdot \text{Mn}_{0.133}$ . Thus, it complimented the findings of the EDX spectroscopy. It also confirmed that Mn content was quite significant and considerable amount of oxygen vacancies were present in nanowires.

### b. Growth Mechanism:

This paper is based mainly on the structural, optical and magnetic properties of Mn doped  $\text{Zn}_2\text{SiO}_4$  nanostructures. However, it is also important to briefly discuss the mechanism of growth of  $\text{Zn}_2\text{SiO}_4$ :Mn nanowires. The formation of the catalyst liquid droplet plays a key role in the growth of nanowires in the VLS mode of growth. In the present case, it is believed that Cl after decomposing from  $\text{MnCl}_2$  reacted with the Si surface and etched it randomly making the substrate surface porous and rough. Simultaneously, Mn and Zn vapors were constantly deposited on the surface and formed the Mn-Zn-Si alloy catalyst droplet. The formation of the Zn-Si alloy droplet as a nucleation site is quite favorable as the eutectic temperature of Zn-Si alloy is 420 °C. This created ideal conditions for the subsequent growth of  $\text{Zn}_2\text{SiO}_4$  nanowires when Zn and oxygen vapors (the latter in the form of water vapors) arrived simultaneously. Thus, it was thought that the growth of these dense bundles of nanowires was the consequence of the etched Si surface and the formation of Mn mixed Zn-Si droplets as catalyst nuclei for growth. A detailed study has also revealed the formation of patterns on the Si surface due to etching by Cl. The pits formed as a result of localized etching become nucleation sites for the bundled growth. From the structural point of view, it is the property of willemite  $\text{Zn}_2\text{SiO}_4$  to nucleate in bundles. Initially, small threads were formed and quickly aggregated into bundles of threads and transformed further into larger bundles. The aggregated bundles were further transformed into the more complex “flowerlike” structures.

Willemite  $\text{Zn}_2\text{SiO}_4$  is a natural orthosilicate with a phenacite like structure (space group  $R\bar{3}$ ), as shown in Figure 4(a). In this structure,  $\text{Zn}^{2+}$  ion occupies two different sites both having four oxygen atoms as its nearest neighbors in a slightly distorted tetrahedral configuration shown in Figure 4(b). In the  $\alpha$ -phase, all Zn ions are at tetrahedral sites, while in the  $\beta$ -structure, half of Zn ions are at the tetrahedral sites and half at the octahedral sites.  $\alpha$ - $\text{Zn}_2\text{SiO}_4$  is a stable phase whereas  $\beta$ - $\text{Zn}_2\text{SiO}_4$  is an unstable phase at room temperature. But when  $\text{Zn}_2\text{SiO}_4$  is doped with Mn, the octahedral coordination favors the  $\text{Mn}^{2+}$  ionic radius, which stabilizes the  $\beta$ -phase. In this crystal structure, two coordination polyherda are formed; Zn-O polyhedra and Si-O polyhedral as shown in Figure 4 (c). When  $\text{Mn}^{2+}$  is doped in  $\text{Zn}_2\text{SiO}_4$ , the Zn-O polyhedra change into Mn-O polyhedra and the coordination environment of Mn-O polyhedra in the  $\alpha$ -phase becomes different from that in the  $\beta$ -phase.

### c. Photoluminescence Spectroscopy:

As discussed earlier, occupation of Mn in the two polymorphs did not bring any significant change in the structural properties due to matching ionic radii and coordination numbers (0.60 Å for  $Zn^{2+}$  and 0.66 Å for  $Mn^{2+}$  (CN = 4)). The PL spectra of the Mn doped  $Zn_2SiO_4$  nanowires taken at room temperature (RT) and at 10 K (LT) are shown in Figure 5 (a), which were significantly different and gave an insight into the origin of the difference in the electronic band structure of the two phases. The signatures of the two polymorphs were quite distinguishable in the low temperature photoluminescence spectroscopy studies, with the  $\alpha$ - $Zn_2SiO_4$  phase emitting green light (530 nm) and the  $\beta$ - $Zn_2SiO_4$  phase emitting yellow light (570 nm) due to modified electronic band structure. In addition, a broad band centered at 660 nm (red band) was also observed. The red emission was quite weak and appeared only as a broad weak bump centered around 670 nm in LT PL spectra. The room temperature PL spectrum, however did not show distinctly the yellow emission band (probably merged into red), but showed a very broad and strong band in red, much stronger than the band observed at 530 nm. It is well established that it is not possible for pure  $Zn_2SiO_4$  to emit in the visible region, contrary to which a broad multi band spectrum in the visible region was observed. The emergence of green and yellow emission bands were ascribed to the states formed due to  $Mn^{2+}$  doping in the  $\alpha$ - and  $\beta$ -phases of  $Zn_2SiO_4$ , however, the presence of the red band was unexpected. A clear difference in the emission was also observed from green to red in the fluorescent microscope images as shown in the inset of Figure 5 (a). It was anticipated that simultaneous substitution of  $Mn^{2+}$  at both  $Zn^{2+}$  and Si sites in the  $\alpha$ -phase and change of the oxidation state from  $Mn^{2+}$  to  $Mn^{4+}$ , respectively, caused Mn ions to couple through Zener double exchange interactions in the form of Mn-O-Mn. The red emission, due to doping of  $Mn^{4+}$  ion at the Si site, was weak at low temperatures as the exchange coupling was weak, as seen in low temperature PL spectra in Figure 5 (a). It is well known that the exchange coupling becomes stronger at low temperatures in the conventional ferromagnets [42-43]. However, in dilute magnetic semiconductors, the exchange coupling becomes weaker at low temperatures, which leads to a strong paramagnetic response, which was indeed observed in the M-H data presented in the next section.. Thus, the emergence of paramagnetic response observed at low temperatures in present nanostructures confirmed the weakening of exchange coupling.

In both phases ( $\alpha$  and  $\beta$ ), the radiative emission is attributed to the  $4T^1$ - $6A^1$  transition within the  $d$ -electrons of the  $Mn^{2+}$  ion as the selection rules do not allow the spin flip transition. Excitation to the  $4T^1$  level occurs after absorption of the incident photon by the  $Mn^{2+}$  in its ground state, leading it to its oxidation state of  $Mn^{3+}$  and the promotion of an electron into the conduction band of the host silicate as described in the following relation (Eq. 1):



Electrons in the conduction band then relax to the  $4T^1$  excited state through non radiative processes, followed by the radiative transition to  $6A^1$  state ( $4T^1 \rightarrow 6A^1$ ) to emit green light at 525 nm and yellow luminescence at 570 nm corresponding to the  $\alpha$ - and  $\beta$ -phases, respectively. The origin of the different spectroscopic properties of the two phases has been ascribed to different Mn sites within the host  $Zn_2SiO_4$  matrix. The variation of energy of the  $4T^1$  and  $6A^1$  levels as a function of the crystal field in a tetrahedral or octahedral environment have been reported by the corresponding Tanabe-Sugano diagram as shown in Figure 5(b) [44]. A qualitative analysis for the red emission is presented in the following. There are a number of possible mechanisms pertaining to the red emission in the Mn doped  $Zn_2SiO_4$ . The substitution of  $Mn^{2+}$  ion in  $Zn_2SiO_4$  host lattice could lead to two different routes of radiative transitions; one probably due to  ${}^4T_1({}^4G)$ - ${}^6A_1({}^6S)$  transition in  $Mn^{2+}$  ions; or two the  ${}^2E$ - and  ${}^2T_1$ - ${}^4A_2$  transition in  $Mn^{4+}$  ions that were substituted at the Si sites of the  $\alpha$ -phase [45]. Another possibility of the red emission was from the defects created in the host lattice, i.e., excess Zn, Si and/or oxygen vacancies [26]. From the lineshape of the red emission band, which was quite distinct from the yellow band, it was evident that substitution of  $Mn^{4+}$  ions at Si site in the host lattice and structural defect states were the major causes. XPS studies have already confirmed the existence of Si vacancies and excess Zn in the host lattice. The possibility of red emission due to  ${}^4T_1({}^4G)$ - ${}^6A_1({}^6S)$  transition in  $Mn^{2+}$  ions was ruled out as it needed at least two or three times more doping of  $Mn^{2+}$  ion. From the above discussion, it was concluded that difference in luminescence properties originated from the difference in the location of the doped Mn ions in the host lattice, i.e., green emission was due to doping at the tetrahedral sites for the  $\alpha$  phase, yellow emission was due to doping of Mn at the octahedral sites for the  $\beta$  phase and red emission was due to substitution of Mn with Si in the  $\alpha$  – phase and structural defects in the host lattice.

The role of the three bands in carrier storage and escape were further studied by temperature dependent PL spectroscopy. The normalized PL spectra collected at various temperatures from 10 K to 300 K are plotted in Figure 6, where spectra have been stacked vertically for the purpose of clarity. It was observed that the green and yellow bands were sharp and intense at low temperatures and as the substrate temperature increased, intensity of the green and yellow lines dropped significantly. On the contrary, red emission increased with increase in the substrate temperature. The spectra were fitted with three Gaussian functions to determine the peak energy positions, widths and integrated intensities. The temperature dependent PL measurements have shown some unique luminescence features due to proximity of green, yellow and red states such as S-shaped (red – blue – red shift) and inverted S – shaped (blue – red – blue shift) variation in the peak emission energy and W-shaped behavior of the full-width at half-maximum (FWHM) in a wide range of temperature as plotted in Figure 7 (a). The peak energy positions of the three bands (Figure 7 (a)) did not follow the free excitonic behavior [44], which was quite expected. The band at 530 nm (2.34 eV) showed a slight red shift of 18 meV in the range of 10 – 90 K and a strong blue shift of 52 meV up to 300 K. The yellow band, i.e., 570 nm (2.18 eV) band showed inverted S – shaped anomalous behavior. In the low temperature range of 10 – 70 K, it showed a blue shift of 32 meV, but then from 70 – 130 K, it showed a red shift of 22 meV. Again in the range of 130 – 200 K, it showed a strong blue shift of 55 meV and from 200 – 300 K it showed a strong red shift of 61 meV. The red band observed at 660 nm (1.88 eV) showed the S – shaped behavior as first it showed a slight red shift of 9 meV in the range of 10 – 40 K, then in the range of 40 – 70 K, it showed a slight blue shift of 13 meV, then in the range of 70 – 120 K, a strong red shift of 63 meV and a slight blue shift of 29 meV upto 300 K was observed. The variation in the peak position as a function of temperature was a clear indication of the variation of localized crystal field due to transfer of charges. The variation in the peak energy positions were understood on the basis of configuration coordinate model for each bound state. The quantum mechanical picture of the configuration coordinate model leads to the quantized states associated with each  $\text{Mn}^{2+}$  level, which shifts to higher energy when excited with carriers. The blue shift of the peak energy with increasing temperature can be understood by the transitions from higher states in the excited level as the excited states were occupied with raised temperature. There are a number of factors, which could lead to “S” shaped behavior of peak energies. The emission peak energies strongly depended on the concentration of isolated

$\text{Mn}^{2+}$  and paired  $\text{Mn}^{2+}$  ions. At low temperatures, the exchange coupling between the ion pairs was weak, thus luminescence is dominated by the isolated  $\text{Mn}^{2+}$  ions. However, with the increase in temperature, the coupling became strong and luminescence was dominated from the paired  $\text{Mn}^{2+}$  ions. The formation of two polyhedra created a strong crystal field between two Mn - Mn ions due to exchange coupling, which led to the red shift of  ${}^4\text{T}^1\text{—}{}^6\text{A}^1$  optical transition, as can be seen in the Tanabe-Sugano diagram, where with the increase in the splitting ( $x$ -axis) the  ${}^4\text{T}^1\text{—}{}^6\text{A}^1$  optical transition ( $y$ -axis) showed the red shift as specifically marked by an arrow in Figure 5(b). This also led to red shift of 530 nm peak as shown in Figure 7 (a). Another very important factor was the excitation of carriers in the excited states, which affected the configuration space. However, red shift was explained by considering the relaxation from excited states to the ground state via phonon emissions. Figure 7 (b) shows the variation of peak widths as a function of temperature, which also showed anomalous or unusual behavior and was attributed to the variation in the carrier concentration as discussed in the following section.

The integrated intensities showed unusual behavior with temperature as all bands showed initially an increase in the intensities and maximized at some characteristic temperatures and then dropped as shown in Figure 7 (c). It was interesting to note that integrated intensities of bands at 530 nm, 570 nm and 660 nm peaked at around 66 K, 50 K and 86 K, respectively. The increase in the intensity with the increasing temperature was a signature of the Berthelot kind of behavior, which was a clear indication that states were in the proximity of each other and acted as reservoirs and escape routes for each other. The strong interaction of these states was responsible for the Berthelot type behavior of the integrated intensities in the Arrhenius plots of three states as plotted in Figure 8 (a-c). The existence of defect states, e.g., the presence of excess Zn (introducing dangling bonds at the surface leading to band tail states) and Si and O vacancies also played an important role in the Berthelot kind of behavior. Thus, fitting was done to extract the activation and escape energies of these states. The percentage weight of each component to the total integrated intensity is also plotted in Figure 8 (d) as a function of  $(k_{\text{B}}T)^{-1}$ . It was observed that at low temperature, luminescence from 570 nm ( $\beta$ -phase) states was stronger than 530 nm ( $\alpha$ -phase) states and 660 nm. This was interesting and quite expected as it could lead to draw a conclusion that  $\beta$ -phase was in the vicinity of  $\alpha$ -phase and at low temperature carriers transferred efficiently to the lowest states, which were radiation efficient. However, at raised

temperature, the transfer process reversed and the luminescence intensity of green band ( $\alpha$ -phase state) increased. The weighted luminescence intensities of the two bands (green and yellow) remained constant as the temperature increased and then dropped drastically at elevated temperatures (around 60 – 70 K). Interestingly, the weighted intensity of 660 nm (defect states) increased drastically, which clearly indicated the transfer or relaxation route of carriers from the two states (green and yellow) to the defect states (red). A simplistic picture of possible non-radiative (upward downward) and radiative transitions among these states is shown in Figure 9. The Figure also represents band edge tail states due to defects, e.g., excess Zn, Si and oxygen vacancies.

The Arrhenius plots of the integrated intensities are shown in Figure 8 (a – c) for three bands. The symbols represent the experimental data and the solid curve is the fit of the Berthelot Eqn. given in (2). All three bands displayed similar but abnormal Berthelot type behavior as the temperature was raised. A sharp rise and fall was observed for 530 nm and 660 nm states, while a broad rise and fall was observed for 570 nm band. Arrows marked in Figure 8 represent the maximum intensity achieved with increase in the temperature and the width of the intensity peak is also mentioned in each Figure, which corresponded to the range of temperature for the reverse process. It was interesting to note that intensity of the bands increased by a factor of 4, 2 and about 5 at 63 K, 61 K, and 75 K for 530 nm, 570 nm and 660 nm, respectively. The intensity of 570 nm at 10 K was the highest among all three bands. The behavior of the integrated intensity for all three bands was evaluated and quantified by assuming that the PL decay rates depended on the radiation rates and hopping rates between the neighboring states (530 nm, 570 nm and 660 nm) either directly or through defect states for the Berthelot behavior. Combining these three processes yielded the total integrated intensity variation with temperature for each band [37, 39]:

$$\frac{I(T)}{I_0} = \left[ 1 + \nu_1^* \exp\left(\frac{k_B T}{E_B}\right) + \left(\frac{E_r}{k_B T}\right) + \nu_2^* \exp\left(\frac{E_r - E_{esc}}{k_B T}\right) \right]^{-1} \quad \text{Eq. (2)}$$

where  $I_0$  is the normalization parameter and  $\nu_1^*$  and  $\nu_2^*$  are the effective hopping frequencies of the carriers for radiative emission and hopping between the states, respectively.  $E_r$  and  $E_{esc}$  are the activation energies of radiative emission and escape energy of carriers.  $T_B$  and energy  $E_B$  are

characteristic Berthelot temperature. The energies  $E_r$ ,  $E_{esc}$ , and  $E_B$  are the energies of the radiative (R) and non-radiative (NR) processes, and the hopping process between the radiative and nonradiative states, respectively. The solid lines in the Figure 8 (a-c) are fits with energies and frequencies as free parameters for the three bands (530, 570 and 660 nm) and are summarized in Table II. The fit gave  $E_{esc} = 70 \pm 3$ ,  $49 \pm 2$  and  $65 \pm 4$  meV for 530 ( $\alpha$ -phase), 570 ( $\beta$ -phase) and 660 nm ( $Mn^{4+}$  substitution in the  $\alpha$ -phase and defect states) bands while the corresponding activation energies for radiation were  $E_r = 1.01 \pm 0.40$ ,  $3.10 \pm 1.10$  and  $1.37 \pm 0.40$  meV for the three bands, respectively. The escape energy of carriers in 570 nm state was high to jump into 530 nm state (approximately 21 meV) and a bit small to jump into 660 nm (16 meV). This meant that with increase in temperature, carriers would prefer to jump into 660 nm state and contribute in the luminescence of 660 nm. In addition, comparatively higher radiation rates for 570 nm was due to the enhanced capture rate as the population of the state increased by downward transition from 530 nm state and upward transitions from the 660 nm state of the carriers either directly or mediated through defect states and it also accounted for a strong luminescence from this state in a wide range of temperature. These results also demonstrated that the 660 nm state benefited most from the depopulation of 530 nm and 570 nm states as carriers thermally excited from these states ended up at the 660 nm state as clearly seen in Figure 8 (d).

The higher capture rate of the 570 nm state resulted from doping of the  $Mn^{2+}$  ion state in the  $\beta$ -phase as compared to that  $Mn^{2+}$  ion state when doped in the  $\alpha$ -phase. This was due to the difference in the coordination geometry of  $Mn^{2+}$  ion for two phases, which would lead to the lowered crystal field in the  $\beta$ -phase compared to the  $\alpha$ -phase. In the  $\beta$ -phase the  $Mn^{2+}$  ion was placed at the octahedral site as a favorable site for the  $Mn^{2+}$  atom for occupation. For these two phases, the electron density was expected to be high surrounding the silicon atom in  $\beta$ -phase as compared to the  $\alpha$ -phase [19]. The high electron density surrounding the Si atom would then lead to a lower ligand field for the neighboring  $Zn^{2+}$  or  $Mn^{2+}$  ions. The difference in the ligand field around the  $Mn^{2+}$  ion in the  $\alpha$ -phase and in the  $\beta$ -phase led to the observed difference in the escape energy of the carrier in the two states. In addition the existence of defect states in the host lattice had shown drastic effects on the transition probabilities of  $Mn^{2+}$  related transitions.

#### d. Magnetic studies:

Figure 10 shows the magnetic moment of the Mn self doped zinc silicate nanowire bundles corrected for the diamagnetic moment of the Si(100) substrate measured at different temperatures between 60 and 380 K. While the total moment itself decreased with increasing temperature, the degree of magnetic ordering increased. This was evident in the suppression of paramagnetic behavior at high magnetic fields as the temperature was increased. A progressive weakening of the magnetic order from an almost saturated state at 380 K to the typically S-shaped hysteresis curve at 60 K was clearly observed. Table III summarizes the values of the remnant moment  $\mu$  and the coercive field  $H_C$  at different temperatures. Similar results have been obtained by Sonoda and Sasaki et al. on MBE grown (Ga,Mn)N films on sapphire (0001) [47-49].

The finite coercivity and remanence measured at all temperatures indicated the dominance of the ferromagnetic component at low fields, while paramagnetic behavior dominated at high fields and low temperatures. It was imperative to determine whether the observation of ferromagnetism in semiconductors doped with magnetic ions is due to artifacts such as clustering of magnetic impurities, or in fact due to intrinsic effects that existed in dilute magnetic semiconductors (DMS). XPS and PL spectroscopy results presented in previous sections clearly indicated that  $\text{Mn}^{2+}$  ions were incorporated into the tetrahedrally coordinated and the octahedrally coordinated Zn sites of the  $\alpha$ - and the  $\beta$ - phases, respectively. Some  $\text{Mn}^{4+}$  ions were also substituted at the Si sites of the  $\alpha$ -phase, which gave rise to the impurity bands in the energy gap. The radiative transitions observed in PL were thus in part due to the oxidation of the  $\text{Mn}^{2+}$  states to  $\text{Mn}^{3+}$  (530 nm and 570 nm) The system thus hosted Mn cations in mixed valence states of  $2^+$ ,  $3^+$  and  $4^+$  and so could support long range ferromagnetic coupling through Zener double exchange interaction. This exchange was stabilized at elevated temperatures because of the higher carrier densities produced by thermal excitation of carriers as observed in the Berthelot kind of behavior. Effects due to Mn clustering were further excluded as a source of ferromagnetism due to the fact that Mn itself is antiferromagnetic in nature. Even if there was a possibility for Mn to form some ferromagnetic compound with the silicate, the very small clusters would expected to be superparamagnetic, i.e., having no coercivity or remanence. This was clearly not the case as can be seen in Table III. Also, there were no signatures of  $\alpha$ -Mn metal or Mn containing compounds in the XRD spectrum. These results demonstrated the

Zn<sub>2</sub>SiO<sub>4</sub> nanostructures doped with Mn behaved like a dilute magnetic semiconductor, not widely reported.

The magnetic behavior was further studied by performing temperature dependent studies. Figure 11 shows the thermal demagnetization behavior of Mn doped Zn<sub>2</sub>SiO<sub>4</sub> nanowires when the sample was field cooled ( $H = 30 \text{ k}\hat{\text{O}}\text{e}$ ) and then measured during heating in a small field  $H_{\text{meas.}} = 200 \hat{\text{O}}\text{e}$  (curve a) and after zero field cooling and measured while heated in the same manner (curve b). Similar behavior has been reported for DMS systems as in refs. [48, 50] and interpreted in terms of the coexistence of ferro and paramagnetic phases. The data showed that the Curie temperature of the Mn doped Zn<sub>2</sub>SiO<sub>4</sub> nanowires lay well above 380 K, which suggests importance of Mn doped Zn<sub>2</sub>SiO<sub>4</sub> nanowires for applications at and above room temperature. Also there is no evidence of the unblocking of magnetic moments in the entire temperature range investigated, which further excluded the existence of small superparamagnetic clusters as a source of magnetism in these materials. To the best of our knowledge, this is the first report of dilute magnetic semiconducting behavior in Mn doped ZnSi<sub>2</sub>O<sub>4</sub> nanowires.

#### IV Conclusion:

We have successfully synthesized Mn doped Zn<sub>2</sub>SiO<sub>4</sub> nanowires bundles with average diameters of 40-80 nm by using vapor liquid solid (VLS) growth method. Simultaneous occurrence of etching and growth resulted in the Mn doped Zn<sub>2</sub>SiO<sub>4</sub> nanowires. EDS mapping and XPS confirmed the doping of Mn, Zn richness, Si and O vacancies in the synthesized nanowires. XRD patterns showed the growth of mixed zinc silicate phases ( $\alpha$ -Zn<sub>2</sub>SiO<sub>4</sub>:Mn and  $\beta$ -Zn<sub>2</sub>SiO<sub>4</sub>:Mn) with  $\alpha$ -Zn<sub>2</sub>SiO<sub>4</sub> being the major phase. The PL spectroscopy results confirmed the different origin of emission bands as being due to difference in location of the Mn ions: in tetrahedral sites of the  $\alpha$  phase (green emission), octahedral sites of the  $\beta$  phase (yellow emission) and substitution of Mn with Si in the  $\alpha$ -phase (red emission). Strong yellow and green band emissions at low temperature was due to radiative transitions from the isolated Mn<sup>2+</sup> ions and quenching of yellow and green emission bands at elevated temperatures was due to strong coupling between paired Mn<sup>2+</sup> ions, which also led to red shift of the peak energies. Detailed temperature dependent PL analysis showed that the three emission bands followed anomalous Berthelot-type. Escape energy of the carrier was lower and radiation rate was higher in the  $\beta$ -phase as compared to the  $\alpha$ -phase of Mn doped Zn<sub>2</sub>SiO<sub>4</sub> nanowires, which resulted in the

difference of the electron density at the Si atom in the two phases. Finally, the magnetization response observed in the Mn doped  $\text{Zn}_2\text{SiO}_4$  nanowires is reported and the nanowires showed typical DMS behavior as a function of temperature. The Mn doped  $\text{ZnSi}_2\text{O}_4$  nanowires behaved like a dilute magnetic semiconductor with a Curie temperature well above 380 K. The magnetization behavior showed the co-existence of both para- and ferromagnetic phases, with the latter dominating at high temperatures. Finally, it was concluded that these nanowires may find potential application in the novel spintronic and magneto-optical devices.

**Acknowledgements:**

This work was funded by the Higher Education Commission through NRPU grant numbers 261 (UHV chamber) and 1770 (Optical Characterization). Authors are thankful to Prof. Y. Bando and acknowledge the use of TEM facilities at NIMS, Tskuba, Japan.

**References:**

- [1] Kim, B. H.; Hackett, M. J.; Park, J.; Hyeon, T. *Chem.Mater.* **2014**, *26*, 59–71.
- [2] Fang, X. S.; Zhai, T. Y.; Gautam, U. K.; Li, L.; Wu, L.; Bando, Y.; Golberg, D. *Prog. Mater. Sci.* **2011**, *56*, 175–287.
- [3] Wang, H.; Rogach, A. L. *Chem.Mater.* **2014**, *26*, 123–133.
- [4] Zhai, T.; Fang, X.; Liao, M.; Xu, X.; Zeng, H.; Yoshio, B.; Golberg, D. *Sensors* **2009**, *9*, 6504–6529.
- [5] Li, Z.; Cheg, L. N.; Sun, Q.; Zhu, Z. H.; Riley, M. J.; Ajiada, N.; Cheng, Z. X.; Wang, X. L.; Qiao, S. Z.; Smith, S. C.; Lu, G. Q. *Angew. Chem., Int. Ed.* **2010**, *49*, 2777–2781.
- [6] Xu, S.; Wang, Z. L. *Nano Res.* **2011**, *4*, 1013-1098.
- [7] Wang, D. S.; Xie, T.; Li, T. *Nano Res.* **2009**, *2*, 30-46.
- [8] Palmer, L. C.; Stupp, S. I. *Acc. Chem. Res.* **2008**, *41*, 1674-1684.
- [9] Xia, Y.; Yang, P.; Sun, Y.; Wu, Y.; Mayers, B.; Gates, B.; Yin, Y.; Kim, F.; Yan, H. *Adv Mater.* **2003**, *15*, 353-389.
- [10] Yang, Y.; Zhuang, Y.; He, Y.; Bai, B.; Wang, X. *Nano Res.* **2010**, *3*, 581-593 (2010).
- [11] Li, L.; Zhang, Y.; Fang, X.; Zhai, T.; Liao, M.; Sun, X.; Koide, Y.; Bando, Y.; Golberg, D. *J. Mater. Chem.* **2011**, *21*, 6525–6530.
- [12] Zhai, T.; Liu, H.; Li, H.; Fang, X.; Liao, M.; Li, L.; Zhou, H.; Koide, Y.; Bando, Y.; Golberg, D. *Adv. Mater.* **2010**, *22*, 2547–2552.
- [13] Kandarakis, I.; Cavouras, D.; Prassopoulos, P.; Kanellopoulos, E.; Nomicos, C. D.; Panayiotakis, G. S. *Appl. Phys. A: Mater. Sci. & Proc.* **1998**, *67*, 521–525.
- [14] Kang, Z. T.; Liu, Y.; Wagner, B. K.; Gilstrap, R.; Liu, M.; Summers, C. J. *J. Lumin.* **2006**, *121*, 595–600.
- [15] Nersisyan, H. H.; Won, H. I.; Youn, J. W.; Won, C. W. *J. Electrochem. Soc.* **2012**, *159*, B406.
- [16] Wang, W. C.; Tian, Y. T.; Li, K.; Lu, E. Y.; Gong, D. S.; Li, X. *J. Appl. Surf. Sci.* **2013**, *273*, 372–376.
- [17] Wang, X.; Huang, H.; Liu, B.; Liang, B.; Zhang, C.; Ji, Q.; Chen, D.; Shen, G. *J. Mater. Chem.* **2012**, *22*, 5330.

- [18] Lojpur, V.; Nikolić, M. G.; Jovanović, D.; Medić, M.; Antić, Z.; Dramićanin, M. D. *Appl. Phys. Lett.* **2013**, *103*, 141912.
- [19] Bertail, C.; Maron, S.; Buissette, V.; Le Mercier, T.; Gacoin, T.; Boilot, J.-P. *Chem. Mater.* **2011**, *23*, 2961–2967.
- [20] Su, F.; Ma, B.; Ding, K.; Li, G.; Wang, S.; Chen, W.; Joly, A. G.; McCready, D. E. *J. Lumin.* **2006**, *116*, 117–126.
- [21] Diao, C.-C.; Yang, C.-F. *Ceram. Int.* **2010**, *36*, 1653–1657.
- [22] Ye, R.; Ma, H.; Zhang, C.; Gao, Y.; Hua, Y.; Deng, D.; Liu, P.; Xu, S. *J. Alloys Compd.* **2013**, *566*, 73–77.
- [23] Ye, R.; Jia, G.; Deng, D.; Hua, Y.; Cui, Z.; Zhao, S.; Huang, L.; Wang, H.; Li, C.; Xu, S. *J. Phys. Chem. C* **2011**, *115*, 10851–10858.
- [24] C. R. Ronda, T. Amrein, *J. Lumin* **1996**, *69*, 245 – 248.
- [25] A. P. Vink, M. A. de Bruin, S. Roke, P. S. Peijzel, A. Meijerink, *J. ElectroChem. Soc.* **2001**, *148*, E313 – E320.
- [26] D. J. Robbins, N. S. Casewell, Ph. Avouris, E. A. Giess, I. F. Chang, D. B. Dove, *J. Electrochem. Soc.* **1985**, *132*, 2784 – 2793.
- [27] Sohn, K.; Cho, B.; Park, H. D. *Mater. Lett.* **1999**, *41*, 303–308.
- [28] Jiang, Y.; Chen, J.; Xie, Z.; Zheng, L. *Mater. Chem. Phys.* **2010**, *120*, 313–318.
- [29] Peng, K.-C.; Lin, Y.-C.; Liu, S.-J.; Hsieh, K.-L.; Tseng, C.-A.; Lin, J.-C. *Jpn. J. Appl. Phys.* **2013**, *52*, 01AC02.
- [30] Cui, H.; Zayat, M.; Levy, D. *Chem. Mater.* **2005**, *17*, 5562.
- [31] An., J. S.; Noh, J. H.; Cho, I. S.; Roh, H. S.; Kim, J. Y.; Han, H. S.; Hong, K. S. *J. Phys. Chem. C* **2010**, *114*, 10330.
- [32] Yang, Y.; Zhuang, Y.; He, Y. H.; Bai, B.; Wang, X. *Nano Res.* **2010**, *3*, 581.
- [33] Takesue, M.; Shimoyama, K.; Shibuki, K.; Suino, A.; Hakuta, Y.; Hayashi, H.; Ohishi, Y.; Smith, R. L., Jr. *J. Supercrit. Fluids.* **2009**, *49*, 351.
- [34] Kokotov, M.; Bar-Nachum, S.; Edri, E.; Hodes, G. *J. Am. Chem. Soc.* **2010**, *132*, 309.
- [35] Zhou, J.; Liu, J.; Wang, X. D.; Song, J. H.; Tummala, R.; Xu, N. S.; Wang, Z. L. *Small* **2007**, *3*, 622.

- [36] Fang, X. S.; Ye, C. H.; Zhang, L. D.; Wang, Y. H.; Wu, Y. C. *Adv. Funct. Mater.* **2005**, *15*, 63–68.
- [37] Kapoor, M.; Singh, V.; Johri, G. *Phys. Rev. B* **2000**, *61*, 1941–1945.
- [38] Nee, T.-E.; Shen, H.-T.; Wang, J.-C.; Lin, R.-M. *J. Cryst. Growth* **2006**, *287*, 468–471.
- [39] Bhatti, A. S.; Antonov, V. N.; Swaminathan, P.; Palmer, J. S.; Weaver, J. H. *Appl. Phys. Lett.* **2007**, *90*, 011903.
- [40] Street, R. A. *Adv. Phys.* **1976**, *25*, 397–453.
- [41] Hirabayashi, I.; Morigaki, K.; Yamanaka, S. *J. Phys. Soc. Jpn.* **1983**, *52*, 671–676.
- [42] Evans, R. F. L. Coopman, Q. Devos, S. Fan, W. J. Hovorka, O. Chantrell, R. W. arXiv:1406.6214 [cond-mat.mtrl-sci] (2014).
- [43] Huang, E. Y. and Kryder, M. H. *J. Appl. Phys.* **2014**, *115*, 213906.
- [44] <http://wwwchem.uwimona.edu.jm/courses/Tanabe-Sugano/TSSpread.html>
- [45] Takesue, M.; Hayashi, H.; Smith, R. L. *Prog. Cryst. Growth Charact. Mater.* **2009**, *55*, 98–124.
- [46] Varshni, Y. P. *Physica*, **1967**, *34*, 149-154.
- [47] Sonoda, S.; Shimizu, S.; Sasaki, T.; Yamamoto, Y.; Hori, H. *J. Cryst. Growth* **2002**, *237-239*, 1358–1362.
- [48] Sasaki, T.; Sonoda, S.; Yamamoto, Y.; Suga, K.; Shimizu, S.; Kindo, K.; Hori, H. *J. Appl. Phys.* **2002**, *91*, 7911.
- [49] Sonoda, S.; Hori, H.; Yamamoto, Y.; Sasaki, T.; Sato, M.; Shimizu, S.; Suga, K.; Kindo, K. *IEEE Trans. Mag.* **2002**, *38*, 2859–2862.
- [50] Chitta, V. A.; Coaquira, J. A. H.; Fernandez, J. R. L.; Duarte, C. A.; Leite, J. R.; Schikora, D.; As, D. J.; Lischka, K.; Abramof, E. *Appl. Phys. Lett.* **2004**, *85*, 3777.

**List of Figures and Tables:**

**Figure 1:** (a) Low and (b) high resolution SEM images, (c) low and (d) high resolution TEM images of the as synthesized Mn doped  $\text{Zn}_2\text{SiO}_4$  nanowires. Inset in (d) represents the SAED pattern.

**Figure 2:** (a) EDS images taken in the bright field (BF) mode for elemental analysis. Each image has the corresponding element identified in it. (b) X-ray diffraction (XRD) pattern of the as synthesized Mn doped  $\text{Zn}_2\text{SiO}_4$  nanowires. The inset in (b) shows the magnified range of the pattern to show diffraction peaks of both  $\alpha$  and  $\beta$  phases.

**Figure 3:** (a) XPS survey scan of the Mn doped  $\text{Zn}_2\text{SiO}_4$  nanowires. (b-e) shows the high resolution spectrum of Zn – 2p, O – 1s, Si – 2p and Mn – 2p regions, respectively. The extracted information from the XPS spectra is given in Table I.

**Figure 4:** (a) Unit cell of  $\alpha\text{-Zn}_2\text{SiO}_4$ , (b) local coordination geometry of two distinct sites Zn(1) and Zn(2) of  $\alpha\text{-Zn}_2\text{SiO}_4$ . (c) Coordination polyhedra of the  $\alpha\text{-Zn}_2\text{SiO}_4$  viewed down the c-axis. Si filled tetrahedra are shown in blue while zinc filled tetrahedra are shown in green.

**Figure 5:** (a) PL spectra of Mn doped  $\text{Zn}_2\text{SiO}_4$  nanowires taken at room temperature (300 K) and 10 K. The inset shows the fluorescence microscope image clearly demonstrating the emission of multi colors. (b) The Tanabe-Sugano diagram for  $d^5$  configuration showing possible  $\text{Mn}^{2+}$  transitions ( ${}^4\text{T}^1$  to  ${}^6\text{A}^1$ ) as a function of splitting [34].

**Figure 6:** Normalized PL spectra as obtained from Mn doped  $\text{Zn}_2\text{SiO}_4$  nanowires taken at various temperatures. The spectra are stacked vertically for clarity

**Figure 7:** Plots of variation of (a) energy peak positions; (b) FWHM and (c) integrated intensities of three bands as a function of temperature as determined from the fitting of three Gaussian functions to the PL spectrum.

**Figure 8:** (a-c) Arrhenius plots of the integrated intensities of the three bands (a) 530 nm, (b) 570 nm, and (c) 660 nm. Solid symbols represent the experimental intensities. The curves are the fits of Eq. (2) to extract hopping rates, radiative, non-radiative rates and activation energies, given in Table II. (d) Weight percentage of integrated intensities of the three bands as a function of  $(kT)^{-1}$ .

**Figure 9:** Energy band diagram of the Mn doped  $Zn_2SiO_4$  nanowires showing three band gap states ( $E_G$  (530 nm),  $E_Y$  (570 nm), and  $E_R$  (660 nm) corresponding to  $Mn^{2+}$  doping at  $Zn^{2+}$  site of the  $\alpha$ ,  $\beta$  phases and at Si site of the  $Zn_2SiO_4$  as discussed in the text. “R” and “NR” represent the radiative (solid arrows) and non-radiative (dashed arrows) transitions.

**Figure 10:** Magnetic moment of  $Zn_2SiO_4:Mn$  nanowires as a function of magnetic field corrected for the diamagnetic moment of the Si(100) substrate.

**Figure 11:** Thermal demagnetization measurements of Mn doped  $Zn_2SiO_4$  nanowires: (a) after field cooling in 30 kOe and (b) after zero field cooling. Both curves have been measured in  $H_{meas.} = 200$  Oe during heating from 55 – 400 K.

**Table I:** Percentage composition of elements as calculated from XPS results.

**Table II:** Extracted parameters from the fitting of Berthelot Equation for the three bands.

**Table III:** Remnant moment and coercivity of Mn doped  $ZnSi_2O_4$  nanowires at various

Figure 1:

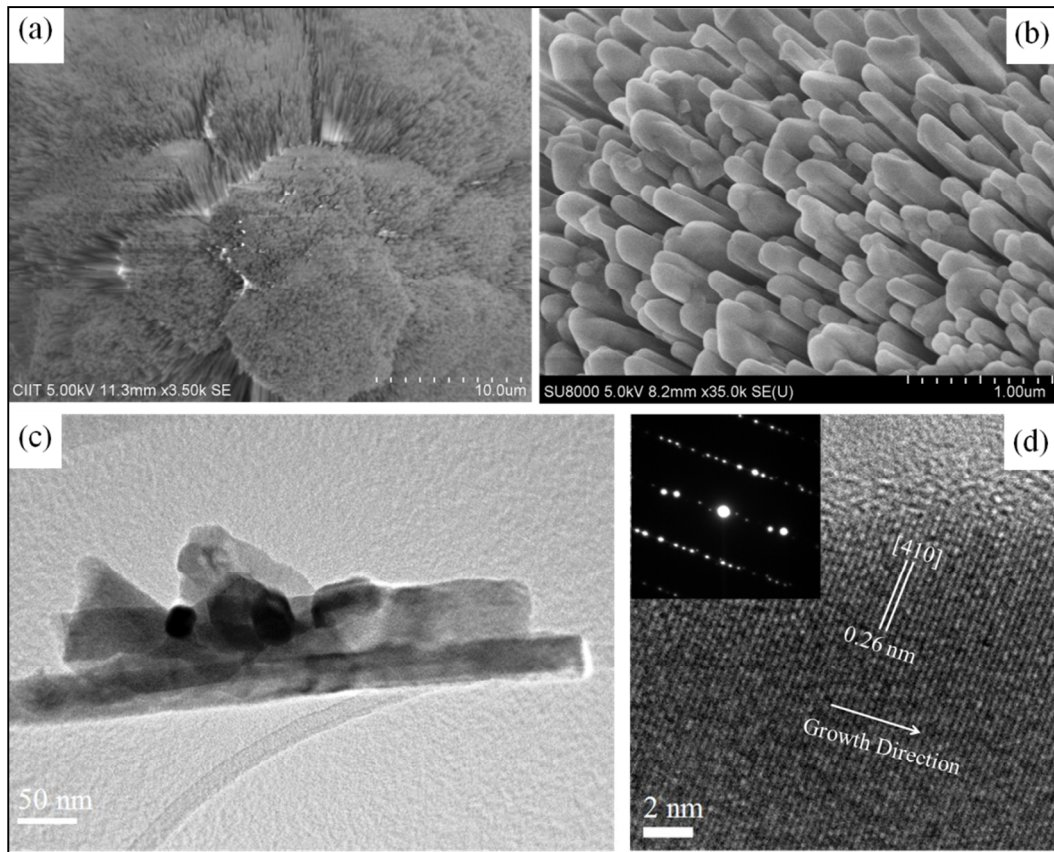


Figure 2:

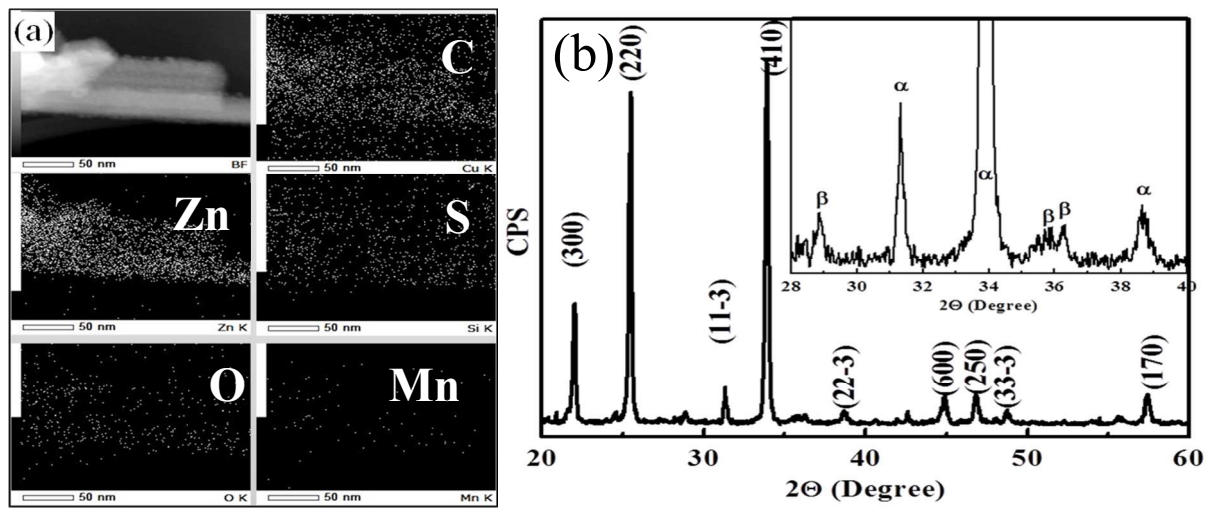


Figure 3:

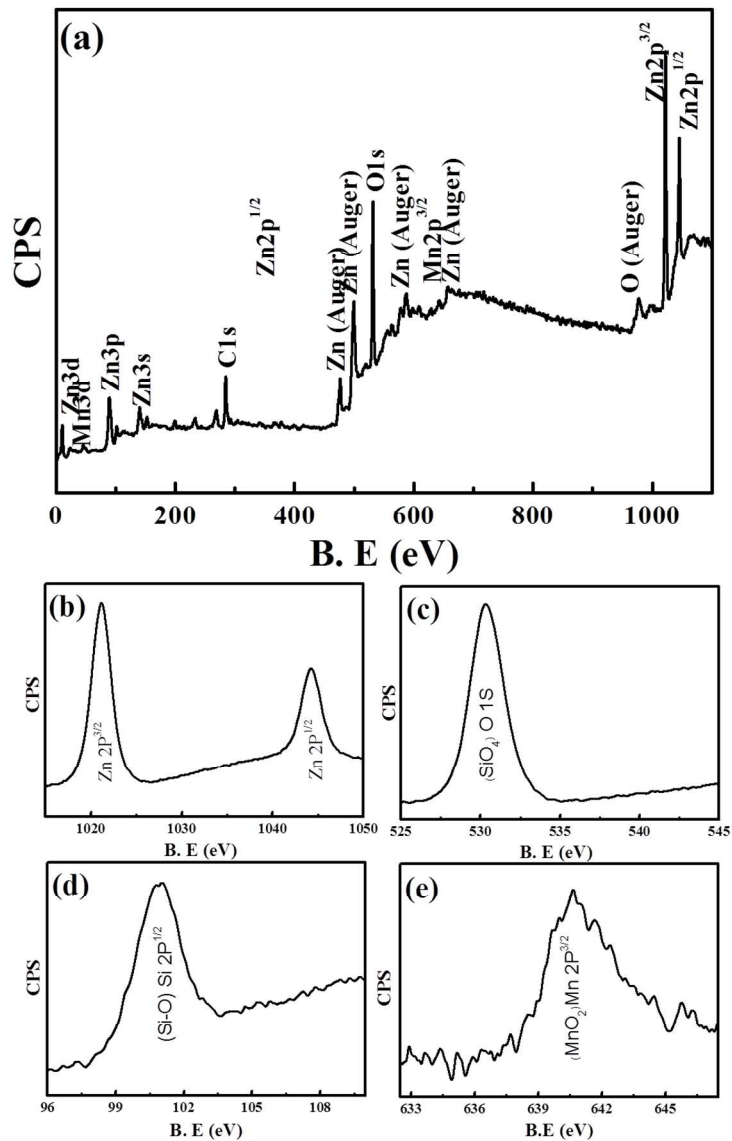


Figure 4:

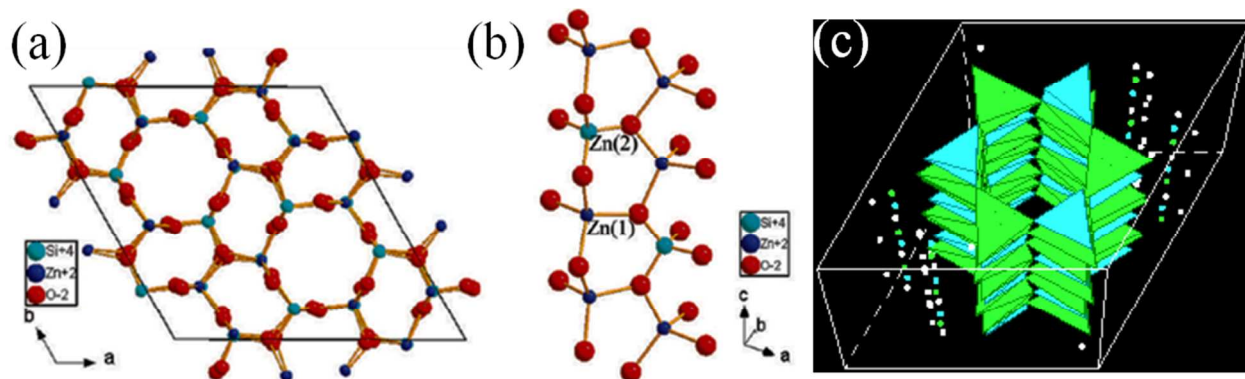


Figure 5:

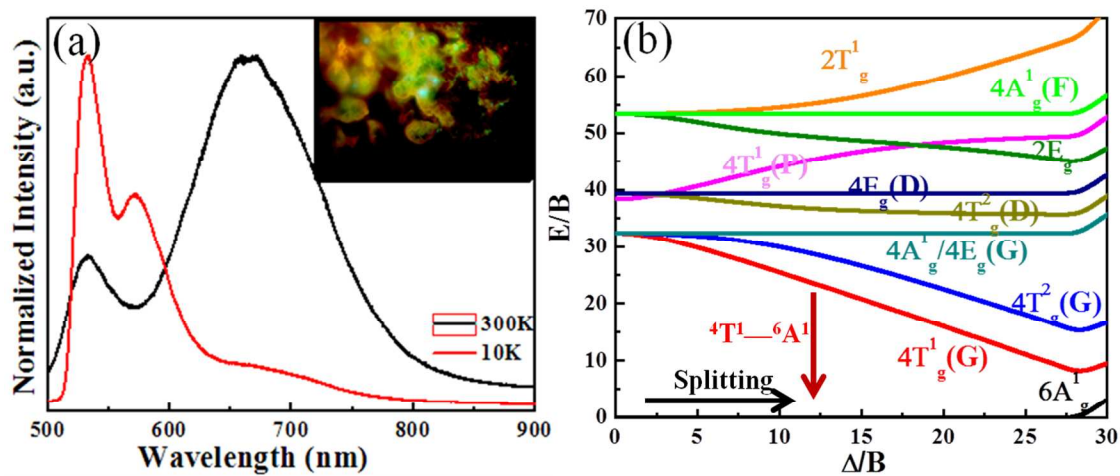


Figure 6:

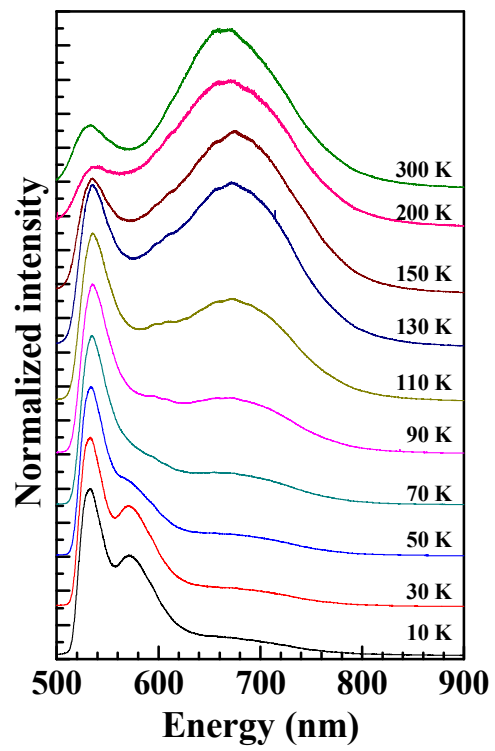


Figure 7:

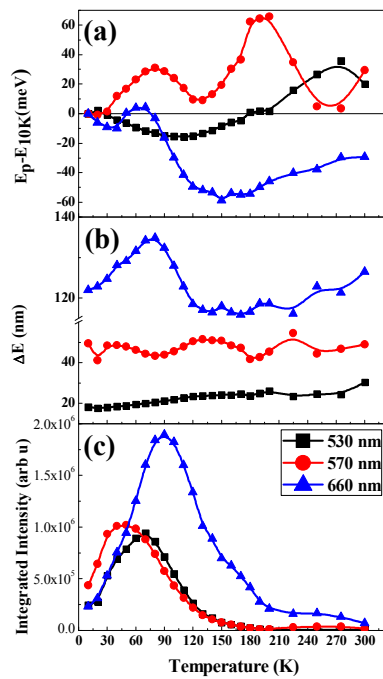


Figure 8:

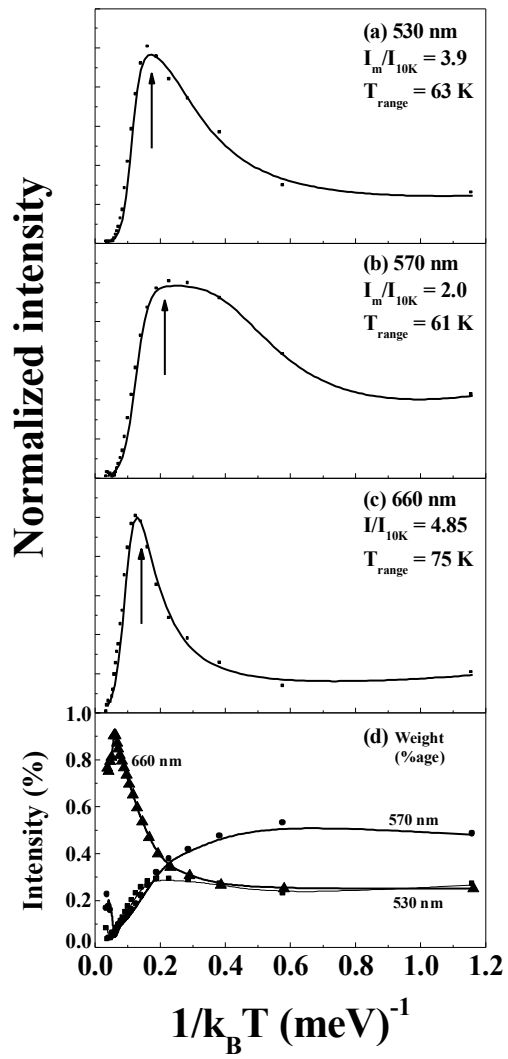


Figure 9

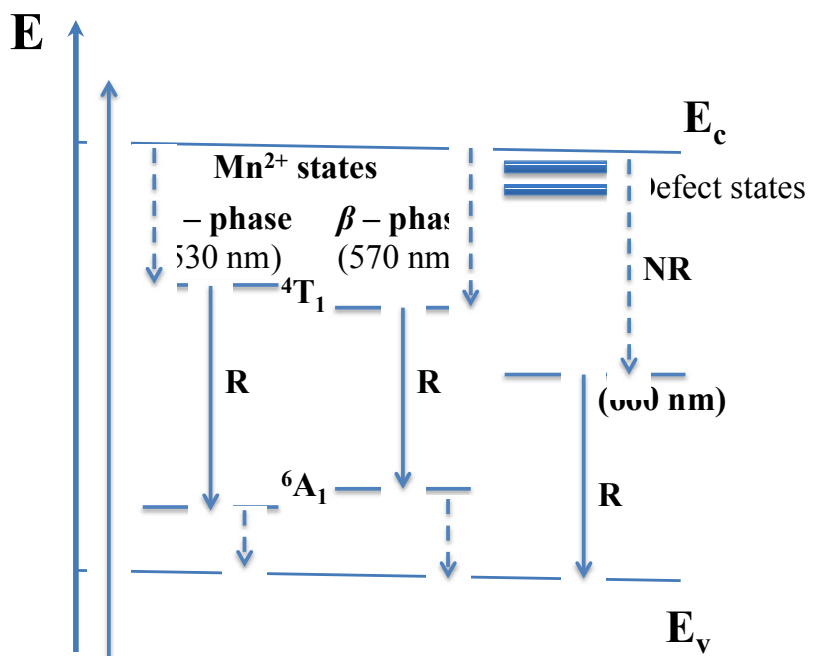


Figure 10:

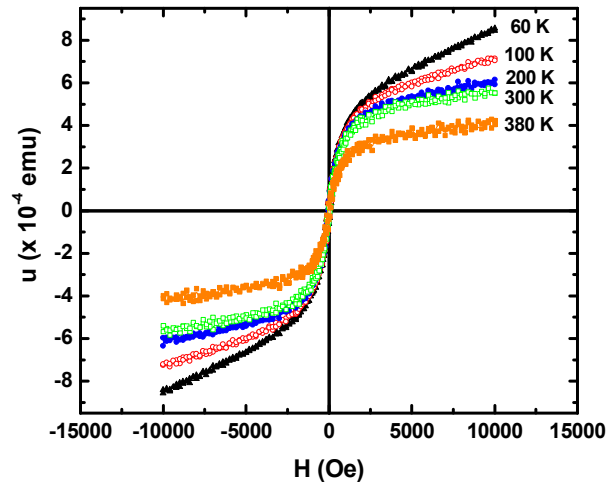


Figure 11:

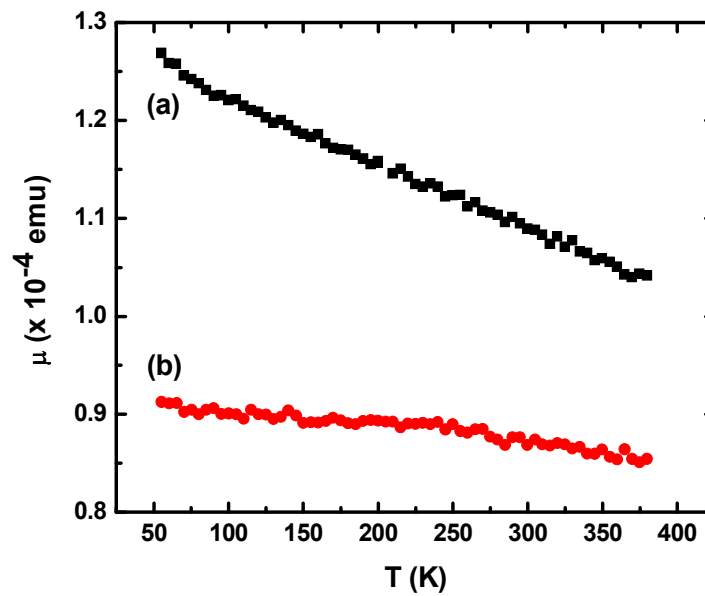


Table I:

Element	Integrated Intensity (I)	Atomic Sensitivity Factor (ASF)	I/ASF	Stoichiometric ratio
Zn(2p)	103859	4.8	21637	0.2971
Si (2p)	2721	0.27	10081	0.1384
O(1s)	26286	0.66	39828	0.5418
Mn(2p)	3599	2.6	1384	0.0190

Table II:

Parameters/bands	530 nm (2.34 eV)	570nm (2.174 eV)	660 nm (1.879 eV)
$I_0$	1.0053	0.986	1.217
$V_1$	27.191	698.75	49.20
$E_B$ (meV)	-1.1561	-3.0773	-0.741
$E_r$ (meV)	-1.0129	-3.1044	-1.373
$V_2$	2886	708	450
$E_{esc}$ (meV)	70.44	49.90	65.06

Table III:

$T(K)$	$\mu_r (\times 10^{-5} \text{ emu})$	$H_C (\text{Oe})$
60	5.6	88
100	5.6	82
200	5.2	69
300	4.0	60
380	4.3	74